Outstanding strain-hardening of a new metastable β-titanium alloy elaborated by in situ additive manufacturing L-PBF process

H. Schaal, P. Castany, T. Gloriant

Outstanding strain-hardening of a new metastable β-titanium alloy elaborated by *in situ* additive manufacturing L-PBF process

Hugo Schaal[1,2], Philippe Castany[1], Thierry Gloriant[1*]

[1] *Univ Rennes, INSA Rennes, CNRS, ISCR UMR 6226, 35000 Rennes, France*

[2] *SLS France, 32 Boulevard de la Haie des Cognets, 35136 Saint-Jacques-de-la-Lande, France*

[*]Corresponding author: thierry.gloriant@insa-rennes.fr

Abstract: The Ti-22Zr-9Nb-2Sn (at%) metastable β-titanium alloy was manufactured by *in situ* laser powder bed fusion process from elemental powders. Mechanical characterization via cyclic tensile tests revealed an exceptionally high strain-hardening. Such a strain-hardenability is induced by a massive stress-induced martensitic transformation from the β to the α'' phase.

Keywords: additive manufacturing, titanium alloy, martensitic transformation, strain-hardening

1. Introduction

Metastable β-titanium alloys are considered of great potential for biomedical applications, thanks to their low Young's modulus, preventing stress-shielding effect, and their excellent biocompatibility due to the use of non-toxic alloying elements for the stabilization of the β phase, such as Ta, Nb, Zr… [1-4]. These titanium alloys can also exhibit stress-induced martensitic (SIM) transformation from the bcc β phase to the orthorhombic α'' phase, which can lead to superelastic behaviour and shape memory effect when the transformation is reversible [5-7], or TRIP (TRansformation Induced Plasticity) effect, that can be combined with TWIP (TWinning Induced Plasticity) effect, leading to alloys with large deformation and high strain-hardening capability [8]. Metastable β-titanium alloys obtained by usual melting techniques (cold crucible levitation melting, arc melting, etc…) have been widely studied and discussed since the last three decades, with a focus of interest on the mechanical properties induced by the SIM transformation. Additive manufacturing, and especially the laser powder bed fusion (L-PBF) technique, is of great interest for the medical fields, because of the capability of the process to manufacture very complex parts, and therefore patient specific biomedical devices. However, elaboration of metastable β-titanium alloys by L-PBF process is challenging due to the poor diversity of pre-alloyed powders available for sale, which are mainly commercial alloys (Ti-6Al-4V, CoCr alloys, stainless steels, superalloys…). Some studies have investigated the manufacturing capability of the *in situ* technique, which promotes the manufacturing of parts with a blend of elemental powders instead of pre-alloyed

powders, achieving alloying operation during the scanning of the laser beam [9,10]. This technique seems more suited when it comes to the prospection of chemical compositions with desired mechanical properties, such as alloys that exhibit SIM transformation. However, this method can lead to the formation of unmolten alloying elements in the metallic matrix, such as β-stabilizing elements with high melting point like Ta, Nb and Mo [11,12]. These inclusions can be detrimental to the local chemical homogeneity, and therefore shift the mechanical properties of the fabricated alloys. Consequently, design of experiments (DOE) must be used to optimize the manufacturing parameters, achieving parts with both low porosity and low unmolten particles for a limited number of tries. This optimization relies on the variation of the main parameters that drives the melt pool, which are laser power, speed of laser scanning and hatch distance between two laser tracks. Even though the *in situ* elaboration can lead to dense and homogeneous parts, the use of this technique to obtain biocompatible metastable β-titanium alloys that exhibit SIM transformation has been rarely investigated.

2. Materials and methods

In this study, the Ti-22Zr-9Nb-2Sn (%at) metastable β–titanium alloy was obtained by the *in situ* technique. An SLM 125 HL (SLM solutions Group AG, Germany) was used to carry out the fabrication of the different specimens. Elemental additive manufacturing grade powders of titanium, zirconium, niobium, and tin were used to achieve our powder mix. The blend of powders was performed using a T2F Turbula device, at a speed of 34 rpm, for 2h of blending. The average powder size of the blend of elemental powders used was between 15 and 45 µm. Optimized building parameters presented in Table 1 were selected through a preliminary study by iterative DOE in order to obtain the highest density by using a 67° hatch strategy [13]. Those building parameters provided parts with a density of about 99.5%, with unmolten niobium fraction of less than 0.05% of the parts volume. Those two different quantities were characterized and measured by X-ray µ-Tomography. Regarding the parts manufactured for this study, two different types of specimens were elaborated: for microstructural characterization, 10x10x10 mm^3 cubes were used, and 50x5x2 mm^3 walls were built to extract by electrical discharge machining flat tensile specimens with a gauge section of 3x1 mm^2 and a gauge length of 15 mm. The tensile direction was taken orthogonal to the building direction. Additive manufacturing process are known to induce important residual stress [14,15]. As thermal treatments are an effective way to relieve this residual stress, the as-fabricated samples were stress-relieved at 700°C for 30 min, and then water quenched to maintain the fully-β microstructure. Cyclic tensile tests were performed to characterize the mechanical behaviour of the alloy, with a strain rate of 10^{-4} s^{-1}. Those cyclic tests consist in strain increments of 0.5% followed by stress unloading, up to the rupture of

the specimen. The unloading parts of the curve enable the identification of potential superelastic behaviour. An extensometer was used to measure the deformation of the sample. 10 different specimens were tested and the mechanical performances are presented via the mean value measured along its standard deviation. The microstructure was characterized by X-ray diffraction (XRD), electron backscattered diffraction (EBSD) and transmission electron microscopy (TEM). EBSD analyses were carried out on a JEOL JSM 7100F scanning electron microscope with a step of 0.1 µm and an accelerating voltage of 20 kV. EBSD specimens were prepared by mechanical polishing using SiC papers with decreasing grid size, followed with colloidal silica suspension polishing mixed with H_2O_2 to get a "mirror finished" state. Optical microscopy specimens were prepared the same way, and then chemically etched with a 5% HF, 5% HNO_3 and 90% H_2O (vol) solution. TEM specimens were thinned by a three steps ion milling process with 4 keV, 2 keV and 0.5 keV argon ions using a Gatan PIPS II machine. Texture was investigated through $\{200\}_\beta$ and $\{110\}_\beta$ poles figures acquisition on a Rigaku SmartLab X-ray diffractometer using Cu-$K_{\alpha 1}$ radiation at 40 kV and 50 mA.

3. Results and discussion

Microstructural analyses of the Ti-22Zr-9Nb-2Sn alloy are presented in Fig.1. A fully β microstructure is expected after water quenching for this alloy. Fig.1a confirms this assumption, as it shows the XRD pattern of the specimen, indexed as β phase. Fig.1b details the microstructure of the alloy through EBSD analyses. The IPF-EBSD map exhibits columnar and elongated grains along the building direction. The grains are about 170 µm long, for an average 60 µm width. This microstructure is typical of parts built by L-PBF technique [9,16], due to the thermal gradient and the layer-by-layer building, promoting epitaxial growth along the building direction (BD). The EBSD analysis corroborates the XRD analysis (Fig.1a), as every grain of the microstructure is successfully indexed with β phase. Texture of the specimen is also investigated through EBSD, thanks to the inverse pole figures presented in Fig.1b. The alloy exhibits a strong $<100>_\beta$ texture in the building direction, which is a consequence of the manufacturing conditions. This texture is characteristics of bcc materials elaborated by L-PBF process and was already reported, either by direct observations or by reconstitution from the room temperature phase [17-19]. However, the texture in the tensile direction (TD) does not exhibit preferential direction. As the EBSD analysis relies on a limited population of grains, the texture is also more accurately evaluated using XRD measurements. The pole figures (Fig.1c) and inverse pole figures (Fig.1e) obtained by XRD confirm the strong $<100>_\beta$ texture in the building direction, and the absence of preferential direction in the tensile direction.

Fig.2a shows the engineering stress-strain curve obtained on the Ti-22Zr-9Nb-2Sn sample after cyclic tensile test to rupture. The yield strength and the ultimate tensile strength reach

421±44 MPa and 1049±15 MPa, respectively. A total elongation of 10.4±0.3% is obtained, and the Young's modulus is evaluated at 45±0.4 GPa. It can be noticed that the unloading part of the cyclic tensile curve shows no reversibility, and therefore no superelastic effect. The specimen exhibits very high strain-hardening, as the difference between yield strength and ultimate tensile strength is about 630 MPa. The strain-hardening rate was obtained by the true stress-strain curve, which is shown in Fig.2b. The strain-hardening curve is composed of three different stages, which are highlighted on the graph. During the early deformation domain (stage I), the strain-hardening rate decreases rapidly. Then, as the material undergoes plastic deformation, the strain-hardening rate increases until it reaches a peak (stage II). Finally, the strain-hardening rate decreases until the rupture of the material (stage III). In our case, the maximum strain-hardening rate is obtained at 753 MPa and its value is 14.6 GPa. A high strain-hardening is quite common in metastable β-titanium alloys that exhibit TRIP and/or TWIP effects [8,20]. However, the present strain-hardening rate value is exceptionally higher than those obtained with other metastable β-titanium obtained by conventional melting process such as Ti-12Mo [8], Ti-9Mo-6W [21], Ti-8.5Cr-1.5Sn [22] and Ti-10V-2Al-3Fe [23], where the maximum strain-hardening rate is about 2-2.5 GPa.

The origin of such an outstanding strain-hardening rate is investigated from microstructural characterizations after rupture. Fig.2c displays the superposition of the XRD patterns of the specimens before deformation and after being strained until rupture. It shows a drastic change of microstructure in the deformed state, which is composed of both α'' and β phases. The lattice parameters measured by XRD analysis are a_β = 0.338 nm, and $a_{\alpha''}$ = 0.309 nm, $b_{\alpha''}$ = 0.518 nm and $c_{\alpha''}$ = 0.479 nm. Despite the presence of some peaks of the original β phase, the relative intensity of these peaks indicates that the microstructure is mainly constituted of α'' phase after tensile test. This observation implies that the alloy undergoes stress-induced martensitic (SIM) transformation, and that a large volume fraction of β phase transformed into α'' phase. This SIM transformation is most probably the cause of the high strain-hardening observed on Fig.2a, as the nucleation of the α'' martensitic phase hinders dislocation slip by the multiplication of interphase boundaries.

Post mortem microstructural characterizations were performed to identify the stress-induced martensite responsible for the high strain-hardening observed during mechanical characterization. Fig.3 exhibits optical micrographs and TEM observations performed on specimens after rupture. The microstructure before deformation is shown in Fig.3a, and is composed of columnar β grains. After deformation until rupture, numerous new black strips are clearly visible within the columnar β grains of the microstructure (Fig.3b). It should be stated that the formation of the stress-induced martensitic α'' phase is similar to a germination/growth process [24] which can be described as followed. First, the martensite forms in the initial β grain, followed by a radial development until it come across an obstacle such as grains boundaries. Then, the martensitic laths growth along their thicknesses until an

energetic local equilibrium is reached. Fig.3b displays thin and numerous laths of martensitic α'' phase within the initial β grains, which implies that the thickening of those laths is limited, and that the formation of new α'' laths is favoured in comparison to the thickening of previously formed α'' laths.

TEM bright field image of the specimen microstructure after rupture corroborates this result (Fig.3c), in which α'' martensitic laths are clearly identified. The corresponding selected area electron diffraction (SAED) pattern is presented along the $[113]_{\beta}/[\bar{1}12]_{\alpha''}$ zone axis (Fig.3d). In this diffraction pattern, the brightest diffraction spots belong to the martensitic α'' phase and the weakest ones to β phase. The indexation of this diffraction pattern implies that the α'' martensite observed was formed accordingly to the classical crystallographic relationship between the β and α'' phase and shows no evidence of twinning during deformation. Considering that the average width of the observed martensitic laths is only about 400 nm, it seems that the local equilibrium that drives the growth of α'' laths is quickly achieved, in opposition with the formation of new α'' phase, which seems more significant. The evolution of the microstructure through deformation can explain the evolution of the strain-hardening curve (Fig.2b): The transition between stage I and stage II (Fig.2b) corresponds to the triggering of the SIM transformation, in which α'' laths begin to form in the initial β grains. As the strain increases, more and more laths of martensite appear in the microstructure, generating interfaces, causing the stress to increase. The transition between stage II and stage III corresponds to a slow-down of the transformation rate of the martensitic phase, causing the strain-hardening rate to decrease until rupture as the number of new interfaces in the microstructure does not increase anymore. The formation of the martensitic laths can occur during stages II and III but does not contribute to the strain-hardening effect, as it does not hinder dislocation slip. The exceptional strain-hardening rate of the present Ti-22Zr-9Nb-2Sn alloy is then due to the SIM α'' transformation without any contribution of twin formation, while both effects are mostly observed concomitantly in literature.

Fig.4 displays the strain-hardenability (ultimate tensile strength – yield strength) as a function of maximum elongation of titanium alloys elaborated by the L-PBF technique. This diagram exhibits the highest strain-hardenability for the present Ti-22Zr-9Nb-2Sn alloy compared to other alloys. Only the heat-treated Ti-10V-2Fe-3Al (900°C/30min followed by water quench) [25] shows similar high strain-hardenability due to a combination of TRIP/TWIP effect. The strain-hardening of this latter is however lower than the one obtained in the present study. This implies that twinning does not affect the strain-hardenability as much as the stress-induced martensite α''.

4. Conclusion

As a conclusion, the Ti-22Zr-9Nb-2Sn (%at) alloy was successfully manufactured from a blend of elemental powders thanks to the *in situ* L-PBF technique. After a stress-relieved treatment at 700°C for 30 minutes followed by a water quench, microstructure is composed of fully-β restored columnar grains, with a strong $<100>_{\beta}$ texture along the building direction. The mechanical characterization of the alloy was achieved through cyclic tensile tests. The stress-strain curve displays a very high strain-hardening, with an outstanding maximal strain-hardening rate of about 15 GPa, which is greatly higher than those commonly observed in literature for such alloys. *Post mortem* characterization by XRD and TEM shows that the alloy undergoes a non-reversible stress-induced martensitic transformation during tensile test. As the SIM transformation triggers, the formation of new α'' laths is shown to be important, as their growth is limited. This important formation of new interphase boundaries hinders the dislocation slip and increase the strain-hardening rate.

Acknowledgment

The authors acknowledge the SCANMAT platforms of the University of Rennes for providing access to XRD, SEM and TEM facilities.

References

[1] P. Laheurte, F. Prima, A. Eberhardt, T. Gloriant, M. Wary, E. Patoor, Mechanical properties of low modulus β titanium alloys designed from the electronic approach, J. Mech. Behav. Biomed. Mater., 3 (2010) 565-573. https://doi.org/10.1016/j.jmbbm.2010.07.001.

[2] M. Geetha, A.K. Singh, R. Asokamani, A.K. Gogia, Ti based biomaterials, the ultimate choice for orthopaedic implants – A review, Prog. Mater. Sci., 54 (2009) 397-425. https://doi.org/10.1016/j.pmatsci.2008.06.004.

[3] M. Niinomi, M. Nakai, J. Hieda, Development of new metallic alloys for biomedical applications, Acta Biomater., 8 (2012) 3888-3903. https://doi.org/10.1016/j.actbio.2012.06.037.

[4] S. Miyazaki, H.Y. Kim, H. Hosoda, Development and characterization of Ni-free-Ti-base shape memory and superelastic alloys, Mater. Sci. Eng. A, 438-440 (2006) 18-24. https://doi.org/10.1016/j.msea.2006.02.054.

[5] P. Castany, T. Gloriant, F. Sun, F. Prima, Design of strain-transformable titanium alloys, Comptes Rendus Physique, 19 (2018) 710-720. https://doi.org/10.1016/j.crhy.2018.10.004.

[6] E. Bertrand, P. Castany, Y. Yang, E. Menou, T. Gloriant, Deformation twinning in the full-α″ martensitic Ti–25Ta–20Nb shape memory alloy, Acta Mater., 105 (2016) 94-103. https://doi.org/10.1016/j.actamat.2015.12.001.

[7] D.M. Gordin, F. Sun, D. Laillé, F. Prima, T. Gloriant, How a new strain transformable titanium-based biomedical alloy can be designed for balloon expendable stents, Materialia, 10 (2020) 100638. https://doi.org/10.1016/j.mtla.2020.100638.

[8] F. Sun, J.Y. Zhang, M. Marteleur, T. Gloriant, P. Vermaut, D. Laillé, P. Castany, C. Curfs, P.J. Jacques, F. Prima, Investigation of early-stage deformation mechanisms in a metastable β titanium alloy showing combined twinning-induced plasticity and transformation-induced plasticity effects, Acta Mater., 61 (2013) 6406-6417. https://doi.org/10.1016/j.actamat.2013.07.019.

[9] M. Fischer, D. Joguet, G. Robin, L. Peltier, P. Laheurte, In situ elaboration of a binary Ti–26Nb alloy by selective laser melting of elemental titanium and niobium mixed powders, Mater. Sci. Eng. C, 62 (2016) 852-859. https://doi.org/10.1016/j.msec.2016.02.033.

[10] B. Vrancken, L. Thijs, J.-P. Kruth, J. Van Humbeeck, Microstructure and mechanical properties of a novel β titanium metallic composite by selective laser melting, Acta Mater., 68 (2014) 150-158. https://doi.org/10.1016/j.actamat.2014.01.018.

[11] S. L. Sing W. Y. Yeong, F. E. Wiria, Selective laser melting of titanium alloy with 50 wt% tantalum: Microstructure and mechanical properties, J. Alloys Compd, 660 (2016) 461-470. https://doi.org/10.1016/j.jallcom.2015.11.141.

[12] J. Wang, Y. Liu, C. D. Rabadia, S.-X. Liang, T. B. Sercombe, L.-C. Zhang, Microstructural homogeneity and mechanical behavior of a selective laser melted Ti-35Nb alloy produced from an elemental powder mixture, J. Mater. Sci. Technol., 61 (2021) 221-233. https://doi.org/10.1016/j.jmst.2020.05.052.

[13] H. Schaal, PhD Thesis, INSA de Rennes, France, 2022.

[14] B. Ahmad, S. O. van der Veen, M. E. Fitzpatrick, H. Gao, Residual stress evaluation in selective-laser-melting additively manufactured titanium (Ti-6Al-4V) and Inconel 718 using the contour method and numerical simulation, Addit. Manuf., 22 (2018) 571-582. https://doi.org/10.1016/j.addma.2018.06.002.

[15] Y. Liu, Y. Yang, D. Wang, A study on the residual stress during selective laser melting (SLM) of metallic powder, Int. J. Adv. Manuf. Technol., 87 (2016), 647-656. https://doi.org/10.1007/s00170-016-8466-y.

[16] L. Thijs, F. Verhaeghe, T. Craeghs, J. Van Humbeeck, J.-P. Kruth, A study of the microstructural evolution during selective laser melting of Ti-6Al-4V, Acta Mater., 58 (2010) 3303-3312. https://doi.org/10.1016/j.actamat.2010.02.004.

[17] E. Vasquez, P.-F. Giroux, F. Lomello, A. Chniouel, H. Maskrot, F. Schuster, P. Castany, Elaboration of oxide dispersion strengthened Fe-14Cr stainless steel by selective laser melting, J. Mater. Process Technol., 267 (2019) 403-413. https://doi.org/10.1016/j.jmatprotec.2018.12.034.

[18] L. Zhou, T. Yuan, R. Li, J. Tang, M. Wang, F. Mei, Anisotropic mechanical behavior of biomedical Ti-13Nb-13Zr alloy manufactured by selective laser melting, J. Alloys Compd, 762 (2018) 289-300. https://doi.org/10.1016/j.jallcom.2018.05.179.

[19] M. Simonelli, Y. Y. Tse, C. Tuck, On the Texture Formation of Selective Laser Melted Ti-6Al-4V, Metall. Mater. Trans. A., 45 (2014) 2863-2872. https://doi.org/10.1007/s11661-014-2218-0.

[20] Y. Fu, W. Xiao, D. Kent, M. S. Dargusch, J. Wang, X. Zhao, C. Ma, Ultrahigh strain hardening in a transformation-induced plasticity and twinning-induced plasticity titanium alloy, Scr. Mater., 187 (2020) 285-290. https://doi.org/10.1016/j.scriptamat.2020.06.029.

[21] F. Sun, J. Y. Zhang, M. Marteleur, C. Brozek, E. F. Rauch, M. Veron, P. Vermaut, P. J. Jacques, F. Prima, A new titanium alloy with a combination of high strength, high strain hardening and improved ductility, Scr. Mater., 94 (2015) 17-20. https://doi.org/10.1016/j.scriptamat.2014.09.005.

[22] C. Brozek, F. Sun, P. Vermaut, Y. Millet, A. Lenain, D. Embury, P. J. Jacques, F. Prima, A β-titanium alloy with extra high strain-hardening rate: Design and mechanical properties, Scr. Mater., 114 (2016) 60-64. https://doi.org/10.1016/j.scriptamat.2015.11.020.

[23] Y. Danard, R. Poulain, M. Garcia, R. Guillou, D. Thiaudière, S. Mantri, R. Banerjee, F. Sun, F. Prima, Microstructure design and *in-situ* investigation of TRIP/TWIP effects in a forged dual-phase Ti-10V-2Fe-3Al alloys, Materialia, 8 (2019) 100507. https://doi.org/10.1016/j.mtla.2019.100507.

[24] M. Bignon, E. Bertrand, F. Tancret, P. E. J. Rivera-Díaz-del-Castillo, Modelling martensitic transformation in titanium alloys: The influence of temperature and deformation, Materialia, 7 (2019) 100382. https://doi.org/10.1016/j.mtla.2019.100382.

[25] S. Mantri, M. S. K. K. Y. Nartu, S. Dasari, A. Sharma, P. Agrawal, R. Salloom, F. Sun, E. Ivanov, K. Cho, B. McWilliams, S. G. Srinivasan, N. B. Dahotre, F. Prima, R. Banerjee, Suppression and reactivation of transformation and twinning induced plasticity in laser powder bed fusion additively manufactured Ti-10V-2Fe-3Al, Addit. Manuf., 48 (2021) 102406. https://doi.org/10.1016/j.addma.2021.102406.

[26] B. Vrancken, L. Thijs, J.-P. Kruth, J. V. Humbeeck, Heat treatment of Ti6Al4V produced by Selective Laser Melting: Microstructure and mechanical properties, J. Alloys Compd, 541 (2012) 177-185. https://doi.org/10.1016/j.jallcom.2012.07.022.

[27] L. C. Zhang, D. Klemm, J. Eckert, Y. L. Hao, T. B. Sercombe, Manufacture by selective laser melting and mechanical behavior of a biomedical Ti–24Nb–4Zr–8Sn alloy, Scr. Mater., 65 (2011) 21-24. https://doi.org/10.1016/j.scriptamat.2011.03.024.

[28] Y. J. Liu, Y. S. Zhang, L. C. Zhang, Transformation-induced plasticity and high strength in beta titanium alloy manufactured by selective laser melting, Materialia, 6 (2019) 100299. https://doi.org/10.1016/j.mtla.2019.100299.

Table and figures:

Table 1. Optimized elaboration parameters determined by DOE.

Laser Power	Scanning speed	Hatching space	Layer thickness
200 W	303 mm.s^{-1}	0.06 mm	20 µm

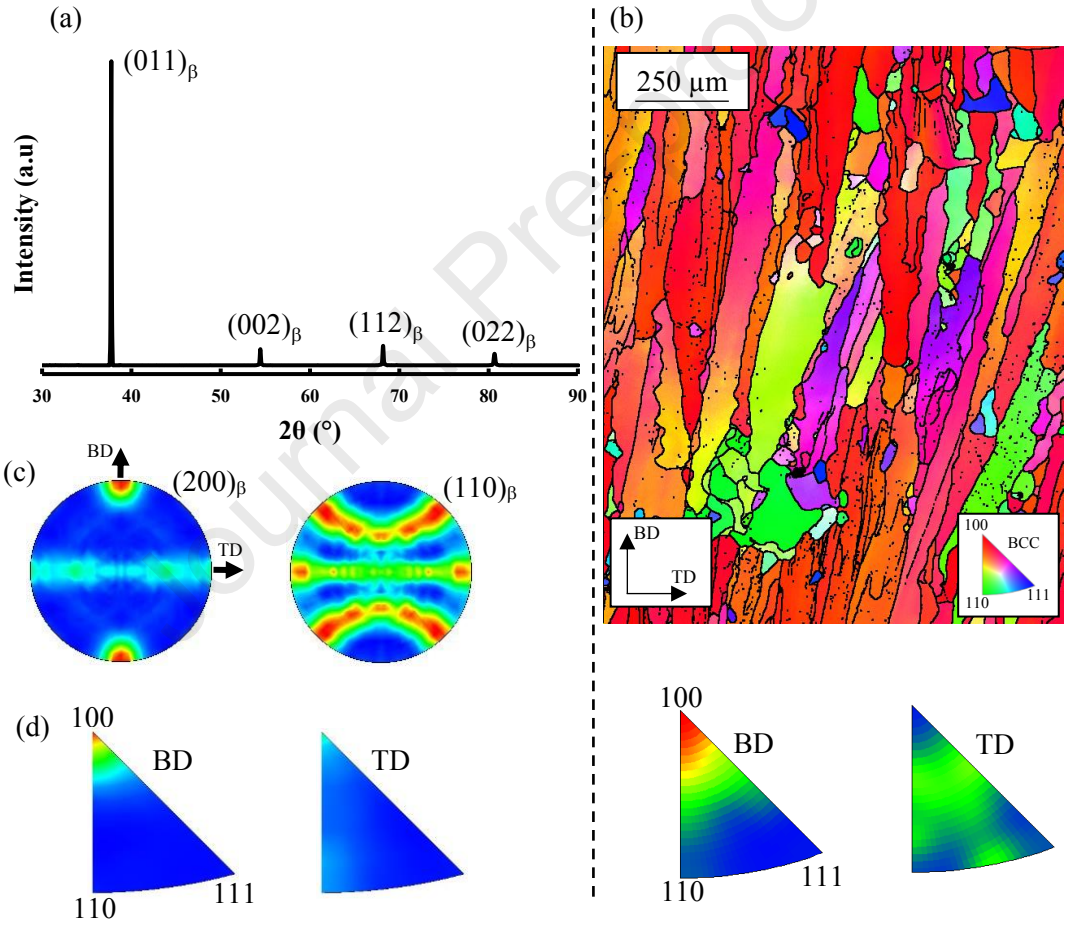

Fig.1. XRD pattern of the Ti-22Zr-9Nb-2Sn alloy (a), IPF-EBSD map of the specimen in the building direction and its inverse pole figures (b). Pole figures (c) and inverse pole figures (d) of the specimen obtained by XRD measurements. BD and TD stands for Building and Tensile Directions.

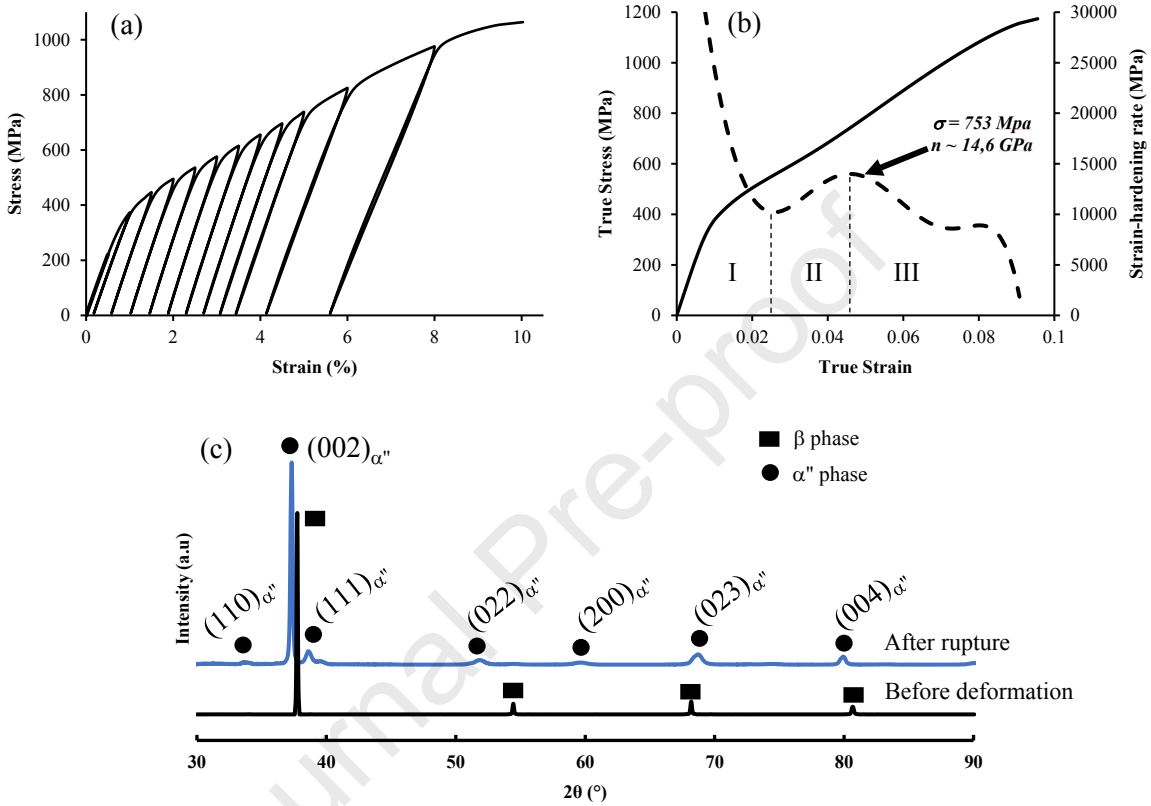

Fig.2. Engineering cyclic tensile stress-strain curve of the Ti-22Zr-9Nb-2Sn sample (a), the corresponding true stress-strain curve and strain-hardening rate curve (dash-line) of the sample (b) and XRD patterns of the sample before deformation and after rupture (c).

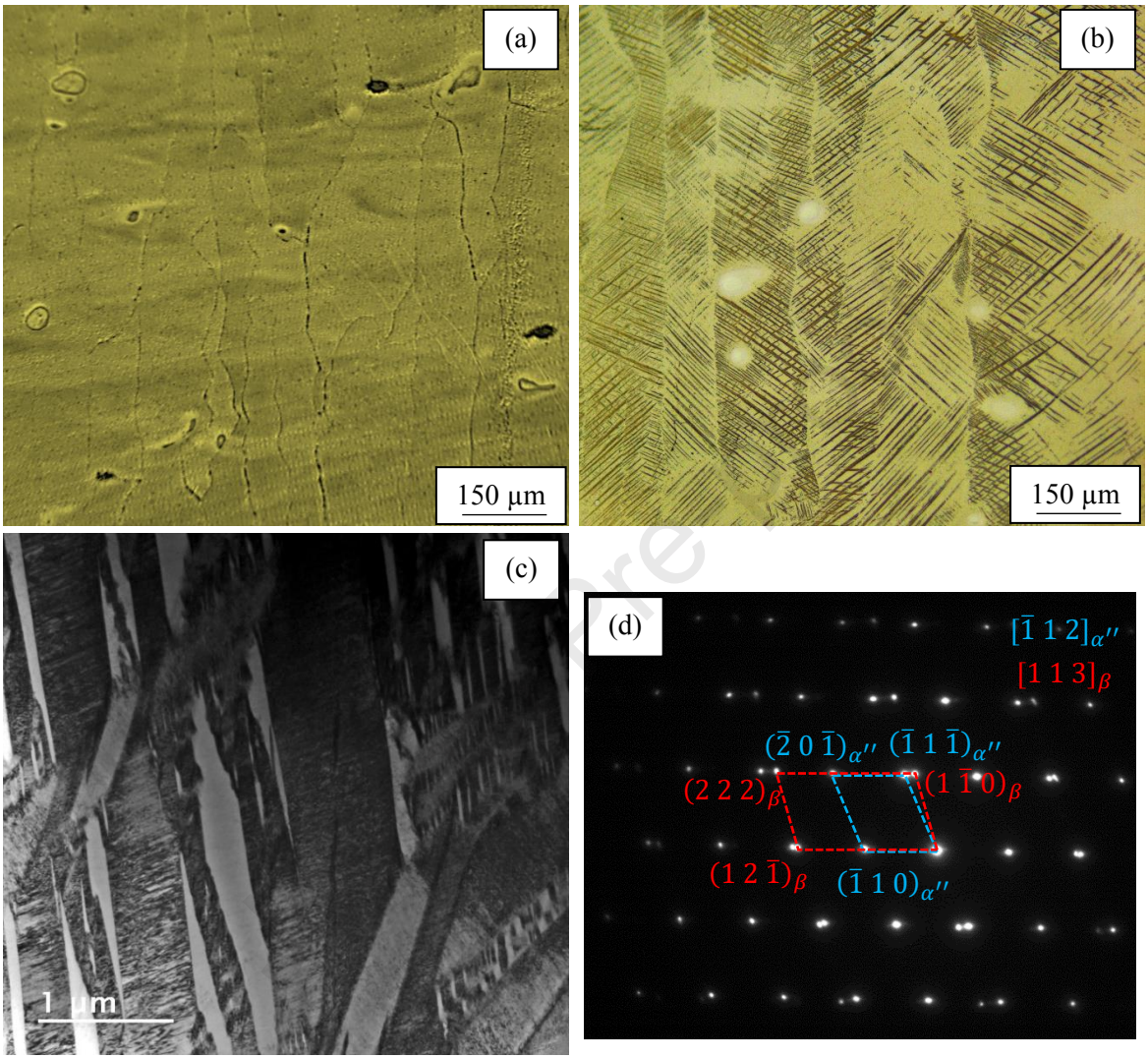

Fig.3. Optical micrograph of the specimen before being deformed (a), optical micrograph of the specimen after rupture showing the α'' martensitic laths in the initial β grains (b), bright-field TEM image of the laths (c), and corresponding indexed diffraction pattern (d).

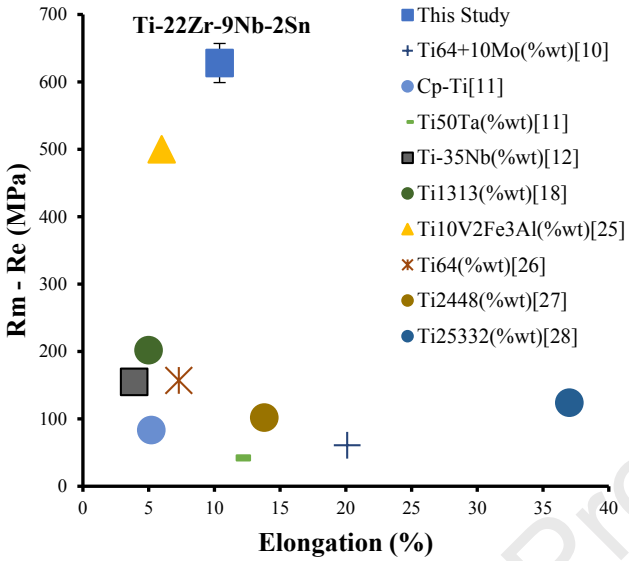

Fig.4. Strain-hardenability of titanium alloys elaborated by L-PBF process as a function of maximum elongation.